

A Computational and Experimental Comparison on the Nucleation of Fatigue Cracks in Statistical Volume Elements

Ebiakpo Kakandar^a, Alejandro Barrios^b, Johann Michler^c, Xavier Maeder^c, Olivier N. Pierron^b, Gustavo M. Castelluccio^{a,*}

^aSchool of Aerospace, Transport, and Manufacturing, Cranfield University, Bedfordshire, MK43 0AL, UK

^bG.W. Woodruff School of Mechanical Engineering, Georgia Institute of Technology, Atlanta, GA, 30332-0405, USA

^cEMPA, Swiss Federal Laboratories for Materials Testing and Research, Laboratory for Mechanics of Materials and Nanostructures, Thun, 3602, Switzerland

Abstract

The failure of micron-scale metallic components present significantly variability as a result of their size being comparable to microstructural length scales. Indeed, these components do not represent the bulk of the material but correspond to statistical volume elements (SVEs). This work investigates the role of SVEs on fatigue crack nucleation with a novel comparison between microbeam experiments and simulations. We recreate multiple microstructural computational realizations to estimate fatigue crack nucleation lives and orientations by means of physics-based crystal plasticity models. We demonstrate a unique approach to validate microstructure sensitive models and quantify the fatigue crack stochasticity associated with small volumes.

Keywords: Crystal plasticity, Mesoscale model, Microstructure, Fatigue, Statistical volume elements, MEMS

1. Introduction

Silicon-base micro-scale components such as micro-electro-mechanical systems (MEMS) have increasingly found widespread applications in diverse industries such as automotive, aerospace, healthcare, defence and consumer electronics [1]. More recently,

new fabrication processes have innovated on metallic MEMS, which can have superior mechanical properties [2] (e.g., better fracture toughness, lower degradation at high temperature). Thus, there is an increasing need to study of the mechanical reliability of microscopic metallic components, among which fatigue failure is a leading concern [3–11].

Metallic MEMS typically have dimensions that are comparable to the microstructure length scales (i.e., a few to hundreds of microns). In such small volumes, only a limited number of microstructural arrangements (e.g., grains, twins) are present, which makes each MEMS a statistical volume element (SVE) [12] rather than a representative volume element (RVE). In other words, two devices will have different mechanical responses because they sample only a subset of the grain morphology, size and orientation distributions [13]. This is particularly important in the study of fatigue loadings, in which cracks tend to nucleate on the surface, which reduces even further the number of grains actively cracking.

Conventional deterministic fatigue models are not appropriate to account for the role of microstructure heterogeneity on fatigue crack nucleation and growth [14]. Instead, microstructure-sensitive approaches such as those based on crystal plasticity finite element modelling (CPFEM) [15,16] are well posed to address these problems. CPFEM explicitly takes into consideration the effect of microstructure heterogeneity to quantify the fatigue response at the microstructural scale under cyclic loading [17]. This approach computes non-local Fatigue Indicator Parameters (FIPs) [18,19], which are computationally friendly surrogates for the fatigue damage driving force at the microstructure scale. FIPs provide a means for quantifying the probability of early crack formation and growth, and have been applied for predicting fatigue life scatter [20].

The computational burden of microstructure-sensitive approaches naturally promotes

the analysis of small volumes with limited number of grain, which correspond to SVEs. On the contrary, most experimental approaches usually rely on large experimental samples that may be considered RVEs. Some experimental approaches [21,22] have considered SVE by restricting the active volume with the introduction of an artificial crack. However, these analyses do not describe the incidence of small volumes on the natural nucleation of cracks. Other approaches [23,24] have employed MEMS to study fatigue initiation, but most microstructural-sensitive modelling approaches consider sample volumes that are significantly smaller than in experiments, which affects the results.

This paper integrates MEMS microresonator fatigue testing and 3D crystal plasticity models with equivalent volumes in order to predict the influence of component size and microstructure heterogeneity on the fatigue crack initiation. The results demonstrate the model ability to both predict and account for the microstructure influence on fatigue nucleation without the need for an explicit calibration of the stochasticity of the process.

2. Experimental Fatigue Crack Nucleation Study of Ni Microbeams

2.1 Microresonator experimental setup: measurement of fatigue crack initiation life

We employ a MEMS microresonator developed by Pierron and co-workers [25,26] to study the transgranular fatigue crack nucleation in Ni microbeams. The microresonator (Figure 1a) is a three-part structure: an electrically grounded Ni microbeam connected to a fan shaped mass, and two sets of interdigitated fingers on each side (for electrostatic actuation and capacitive sensing of resulting motion). The microbeam has dimensions of approximately 60 μm (length) x 12 μm (width) x 20 μm (thickness). The MEMS was electroplated using a conventional, additive-free sulphamate bath (including 405 g/L Ni sulphamate, 7.5 g/L Ni bromide, 97.5 g/L Ni, 37 g/L boric acid) at 30°C, pH = 4, using a direct current (DC) of 20 mA/cm². In sulphamate baths without additives, deposition

parameters, especially current density, affect the amount of deposited impurities (light elements and metallic impurities), which in turn affects texture and microstructure [27–29]. For current densities above 10 mA/cm², the relatively high purity of the electrodeposited Ni (typically above 99.9%) results in a strong out-of-plane <001> texture and columnar microstructure with relatively large grains [27–30]. This is consistent with our microstructure characterization (see 2.3), with most grain widths ranging from 2 µm to 4 µm, as also observed in other studies for current densities of 20 mA/cm² [27–30]. Contrary to the top of the microbeam, which exhibits non-negligible roughness, the sidewalls are mostly smooth [31]. Hence, fatigue damage that emerges on the sidewalls is fully controlled by intergranular variability with minimum contribution from the surface finish [32].

The mechanical monotonic tensile properties have been previously measured using microtensile tests of dog bone shaped specimens [33]: the 0.2% yield stress is $\sim 650 \pm 70$ MPa, the tensile strength is $\sim 875 \pm 25$ MPa, and the ductility exceeds 10%. These properties are in good agreement with another study for Ni sulphamate bath at the same current density (20 mA/cm²), which measured a 0.02% yield stress of 441 ± 27 MPa (our 0.02% yield stress is ~ 450 MPa) and a tensile strength of 758 ± 28 MPa [34]. The large yield stress compared to bulk Ni is likely the result of Hall-Petch strengthening [35], and solid solution strengthening from impurities that can range from 100 to 1000 ppm depending on the bath purity content and deposition conditions [27–29,36].

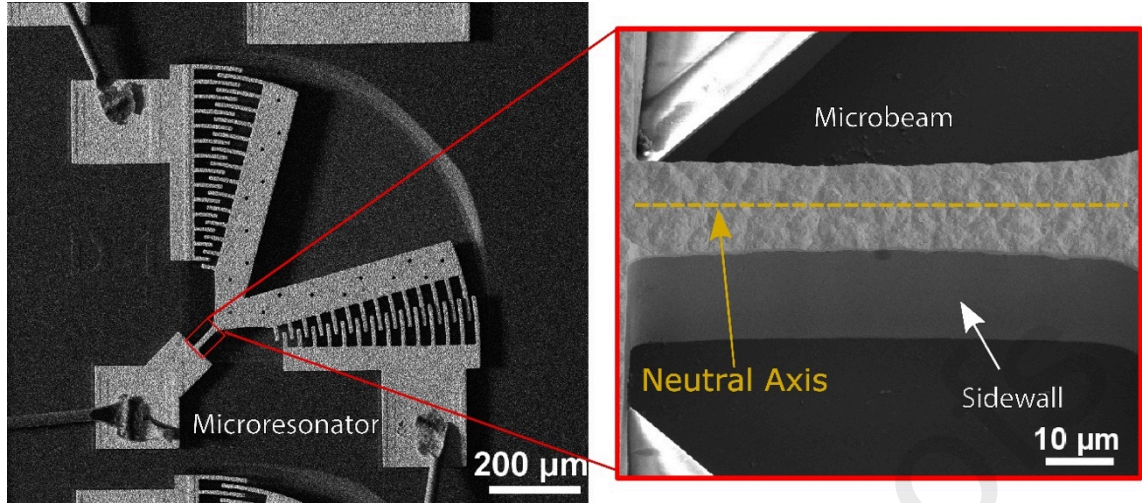


Figure 1. SEM image of a Ni microresonator and a detail of the microbeam (inclined SEM images) [31]. Note the smooth surface on the sidewall, where cracks nucleate upon cycling loading.

The microresonator allows for the electrostatic actuation through one comb structure (via a high sinusoidal input voltage) resulting in a cyclic in-plane fully reversed bending of the microbeam when driven at the structure's resonance frequency (~ 8 kHz). The damping effects and maximum applied input voltage limit the maximum amplitude of rotation to about 28 mrad (resp, 24 mrad) in air (resp. vacuum), corresponding to low plastic strain amplitudes $\epsilon_{pa} < 10^{-3}$ (high / very high cycle fatigue regime). For large enough amplitudes of rotation (> 14 mrad, which corresponds to stress amplitude above 300 MPa), the actuation of the microresonator at resonance results in fatigue damage on the microbeam sidewalls in the form of extrusion/intrusion, and eventually cracks. This damage decreases the microbeam stiffness and, consequently, the resonance frequency, which is measured throughout the fatigue test via the second comb structure. The decrease in f_0 is therefore used as a metric to identify cracking. Fatigue failure of these microbeams typically occurs as two main fatigue cracks, spanning the entire thickness (20 μm), develop on each side of the microbeam and grow towards the neutral axis.

In situ SEM fatigue tests allow for a thorough observation of the evolution of fatigue damage along the sidewalls [31] and show a clear fatigue crack spanning through several

grains along the microbeam thickness direction, formed for a 3-4% decrease in f_0 . Thus, we employ a 1% decrease in f_0 as our criterion for determining the number of cycles to crack the first grain, which will be further validated with finite element models (see section 4). As further justification, an in situ SEM fatigue test was performed and interrupted after 1% decrease in f_0 (see Figure 2a). The sidewalls after the tests (see Figure 2b) show significant fatigue damage in the form of extrusions, intrusions, and possibly cracks. Focused Ion Beam (FIB) sectioning of the microbeam (see section 2.2 for procedure) revealed, on average, that only 1 grain that was fully cracked (see Figure 2c), along with one or two other grains that are partially cracked.

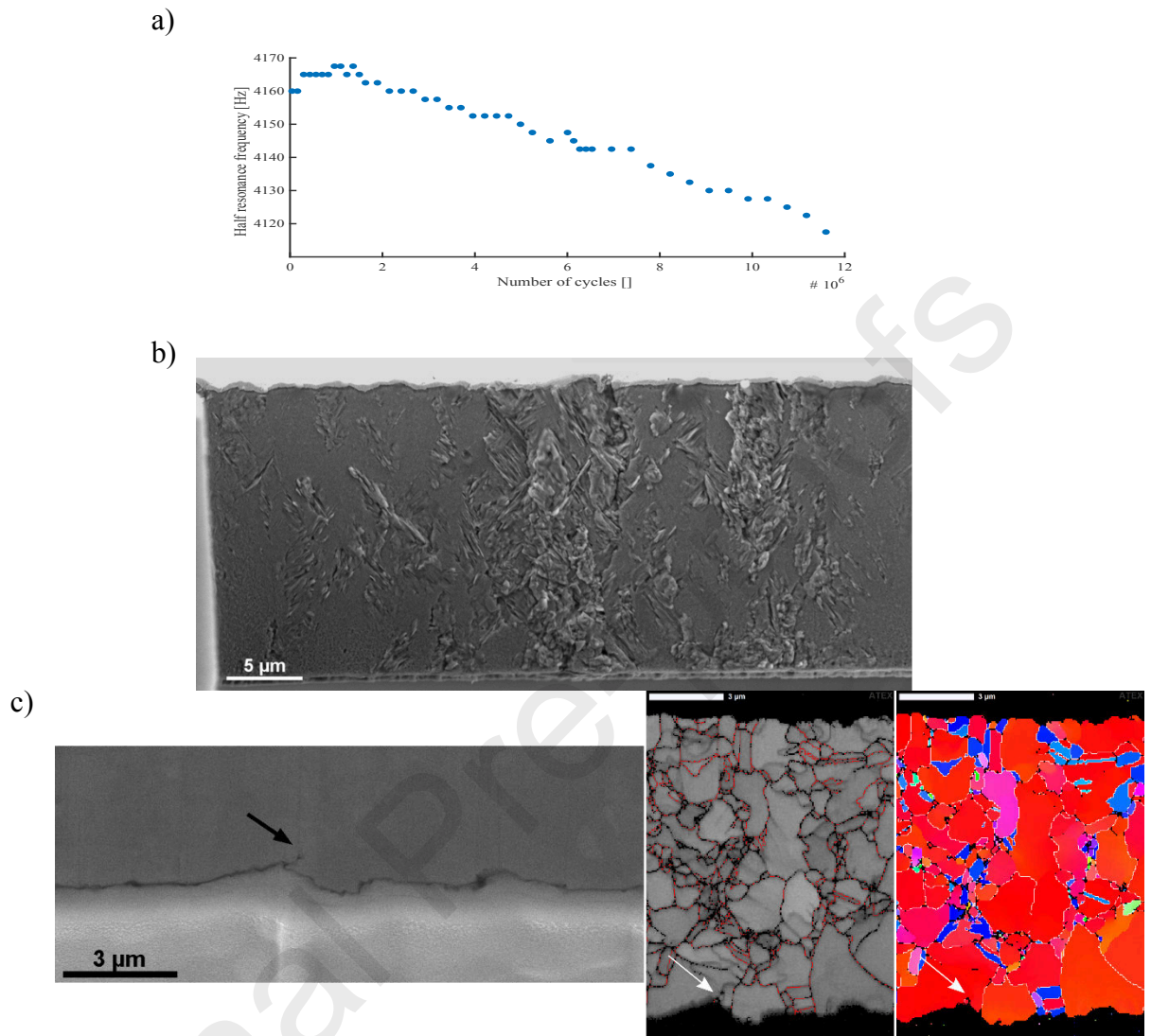


Figure 2- (a) Change in resonance frequency in a microresonator tested at 25.6 mrad rotation and interrupted after 1% frequency decrease (b) fatigue damage in the sidewall of the microbeam (c) FIB cross-section and EBSD scans of the microbeam showing a transgranular crack on one grain .

2.2 FIB Sectioning and EBSD characterization of microstructure and fatigue cracks

Selected microbeams were cross-sectioned along their length (perpendicular to the thickness) using FIB by a depth of about 1.5 μm from the top surface. The microbeam was subsequently polished at a low FIB current in order to obtain a flat surface. The cross-section was positioned in front of an Oxford Instruments Symmetry Electron Backscatter Diffraction (EBSD) sensor and the sample was scanned with a step size of 0.1 nm to a 2D

scan size of $40\text{ }\mu\text{m} \times 15\text{ }\mu\text{m}$, spanning the part of the microbeam where fatigue failure occurs. The microbeam was again cross-sectioned by another $1.5\text{ }\mu\text{m}$ and the procedure was repeated until the whole microbeam was characterized (about 13 cross-sections spanning the entire microbeam thickness ($20\text{ }\mu\text{m}$)). The EBSD data provide microstructure information (distributions of the morphology and size of grains) that informs models with equivalent synthetic microstructures (see 2.3). In addition, the cross-sections enable accurate identification of cracks within grains, which is not possible only based on SEM images of the sidewalls. As an example, the serial FIB sectioning of the specimen shown in Figure 2b only revealed one cracked grain (see Figure 2c) even though numerous extrusions and intrusions are observed on the sidewall. Appendix A presents further examples of cracks and EBSD scans.

2.3. Microstructure characterisation and reconstruction

The microstructure in the microbeam consists of large columnar grains interspersed with smaller equiaxed grains. The morphology, size and orientation of the microstructure was quantified by means of EBSD and processed with Dream 3D [37]. Figure 3 depicts an EBSD map and a pole figure of the microbeam with a strong [001] texture. We consider grains segmented with a five-degree tolerance while voxels belonging to grains with less than 24 voxels and with an orientation confidence of less than 0.1 are removed and added to neighbouring larger grains. Since fatigue cracks tend to initiate from the relatively larger grains [38], we obtained the statistics of the largest area fraction grains consisting of 206 grains with grain size over $1.9\text{ }\mu\text{m}$. The statistics of these grain distributions are then used for creating a SVEs with synthetic columnar grains. The experimental grain size distribution grains truncated at $1.9\text{ }\mu\text{m}$ was fit to a log-normal curve as shown in Figure 4a. The aspect ratios of the real and the synthetic microstructures for the microbeam are

comparable, as shown in Figure 4b and 4c.

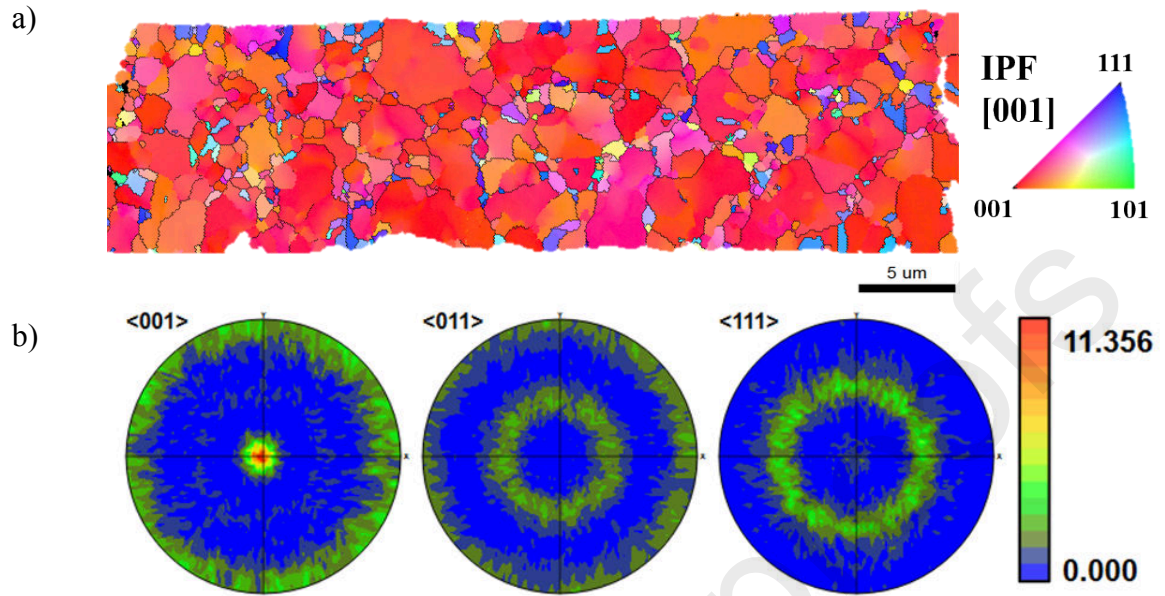


Figure 3. (a) Sample EBSD map and (b) Grain texture (ODF) pole figure obtained from the microbeam.

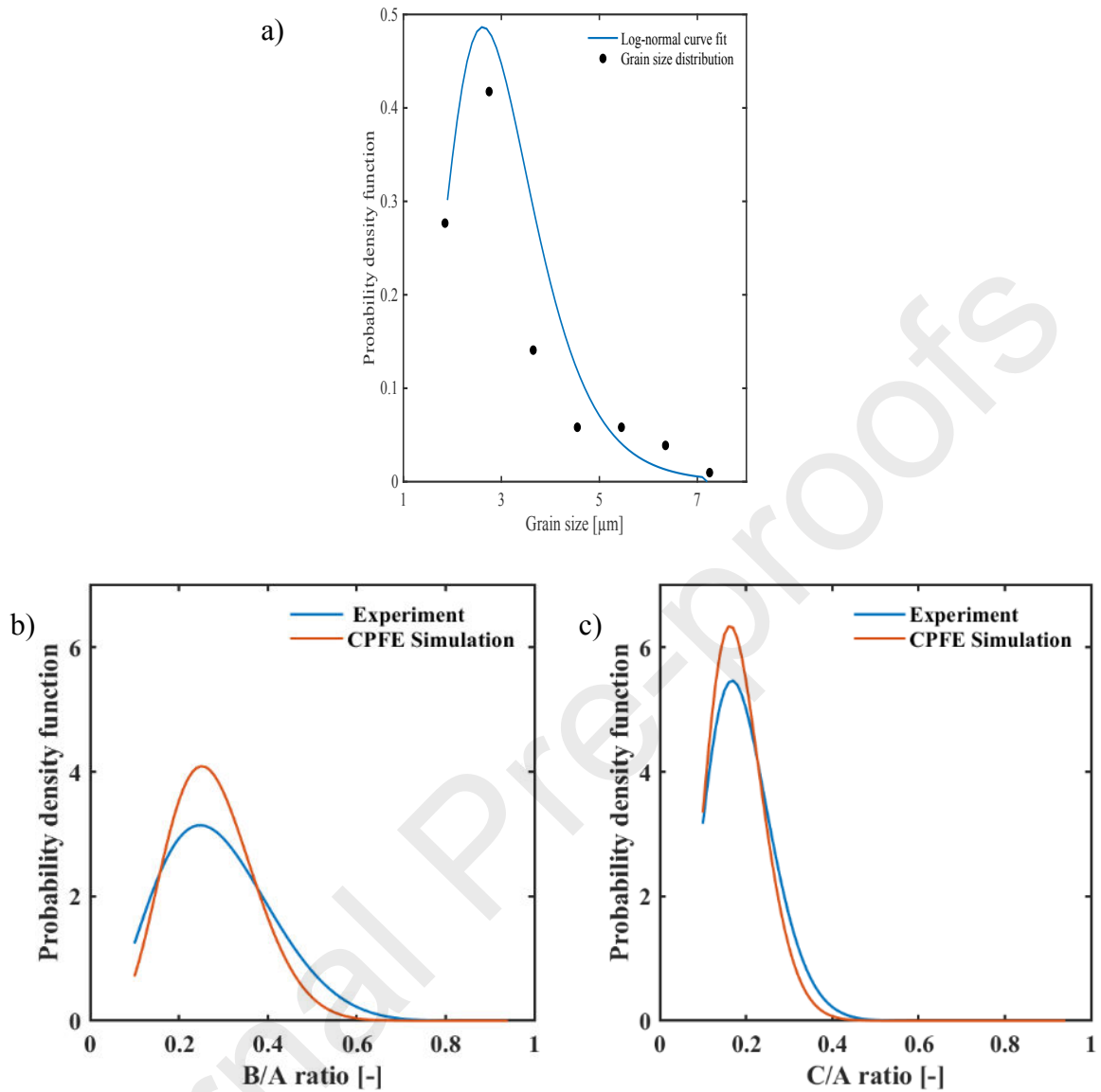


Figure 4. Grain statistics plots showing (a) Grain size distribution of extracted large grains from the 3D EBSD data with the fitted truncated log-normal curve used for creating the SVEs (b) B/A grain aspect ratio (c) C/A grain aspect ratio (A, B and C being semi-major axis of grains).

3. Microstructure-sensitive modelling

3.1 Finite element model

We represent the microbeam with a finite element mesh built with cuboidal reduced integration 8-node linear brick elements (C3D8R) from Abaqus element library (Figure 5a). The microstructure in the microbeam central gauge section (Figure 5b) is recreated

with Dream 3D [37], which informs the statistics of grain morphology and orientation into an in-house Matlab script integrated with Abaqus python scripts. These were used to create 20 meshes with statistically equivalent synthetic microstructures in the gauge section (Figure 5). The scripts also recreate sets of elements that form one-element-thick bands parallel to the crystallographic plane (Figure 5c). These bands serve as a crystallographic regularization length scale [12] in which fatigue cracks nucleate, as explained in the following section.

The simulations apply fully reversed bending to a reference point, to which the nodes at the microbeam free end are kinematically coupled (Figure 5a). Thus, a bending rotation at the reference point creates corresponding bending load in the microbeam. The extreme of the microbeam is constrained from displacing in all directions, as shown in Figure 5. We considered displacement controlled rotation angles of 18, 20, 25 and 30 mrad with a period of 0.00125s, which corresponds to the experimental resonant frequency. For completeness, Appendix B presents the quasi-linear relation between maximum strain and angle of rotation.

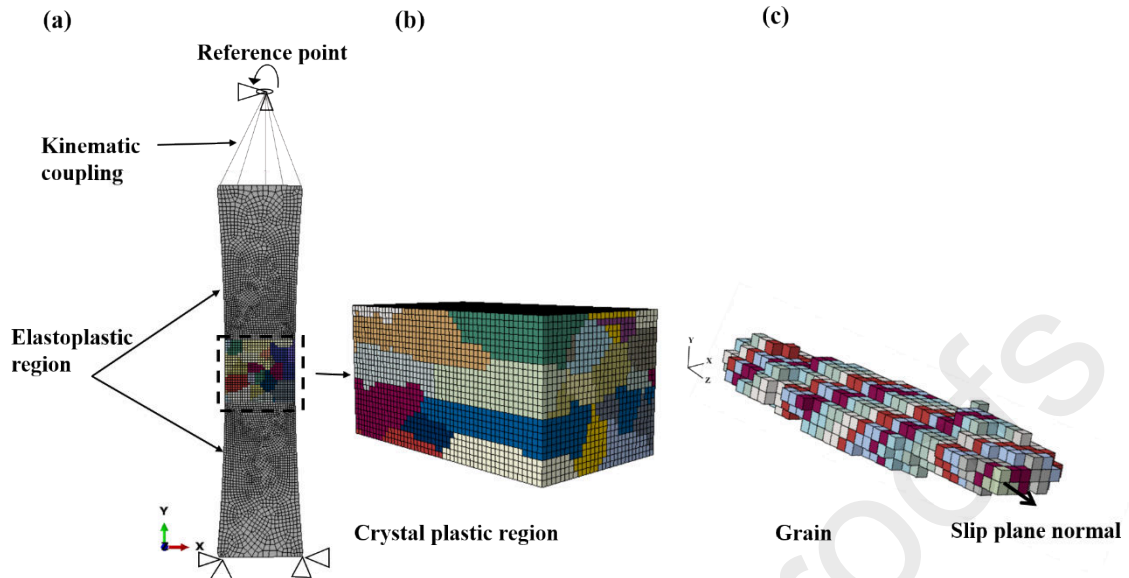


Figure 5. (a) Finite element model of the microbeam. Note the bending load and the different materials for the gauge section and the microbeam extreme sections. (b) Central gauge section presenting one synthetic microstructure realisation of the microbeam. (c) A grain with the color-coded crystallographic bands in which the local FIPs are averaged.

The microbeam gauge section employs a crystal plasticity model and the extreme sections employ an isotropic elasto-plasticity model constructed with the piece-wise experimental stress-strain curve (see Figure 6) and von Mises yield surface criteria. The crystal plasticity formulation was originally designed by Castelluccio and McDowell [40] for modelling FCC metals under cyclic loading and recently reviewed for modelling electroplated Ni microbeams [41]. This constitutive model explicitly conveys dislocation-based hardening mechanisms, which have been independently parameterized. In addition, it considers the contribution from sessile dislocation structures on the back stress. The macroscopic response has been extensively validated for single- and poly-crystalline Ni and Cu. The model was implemented as a user-material subroutine (UMAT) in Abaqus [42] and further details about the formulations are presented in Appendix C. Figure 6a presents the polycrystal cyclic stress-strain curves from simulations at different deformation rates compared with the monotonic experimental results. These simulations correspond to

simple tensile models with 500 cuboidal grains [40], which were informed with the texture from EBSD scans. Overall, the constitutive model agrees with experiments on the elastic and plastic responses and presents a mild strain rate sensitivity, as expected for Ni [43,44].

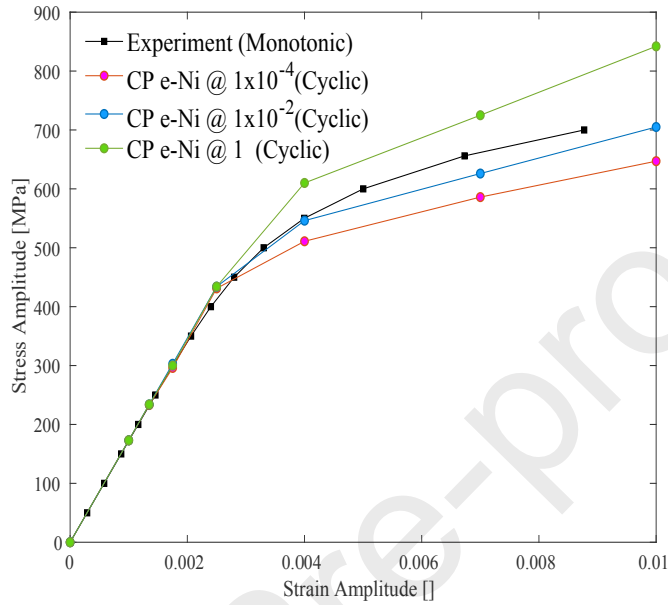


Figure 6. (a) A comparison of the stress-strain curves from monotonic experiment and cyclic deformation from CPFEM at various deformation rates.

3.2 Fatigue crack nucleation model

A convenient and efficient computational prognosis of fatigue crack nucleation relies on surrogate measures of the fatigue cracking driving force [45]. Following the framework proposed by Castelluccio and McDowell [16,39], we compare the fatigue crack nucleation resistance in different grains by surveying fatigue indicator parameters (FIPs) over domains representative of transgranular damage. The Fatemi-Socie [6] FIP is well posed to characterize transgranular cracking, which is driven by the cyclic shear strain range at each slip system ($\Delta\gamma_p^\alpha$),

$$\text{FIP}^\alpha = \frac{\Delta\gamma_p^\alpha}{2} \left(1 + k \frac{\sigma_n^\alpha}{\sigma_y} \right).$$

1

Here, σ_n^α corresponds to the maximum stress oriented normal to the slip plane α , while $\sigma_y \cong 400 \text{ MPa}$ is the macroscopic cyclic yield strength, and $k = 0.5$, as originally proposed by Fatemi-Socie [46]. The FIP in Eq. **Error! Reference source not found.** is computed for each integration point and each octahedral slip system. Next, the FIPs are averaged along mesoscale domains, which correspond to bands parallel to crystallographic planes (see Figure 5(c)). The averaging over bands represents the transgranular damage process zone and mitigates the effects of discretization from the finite elements. The band-averaged FIP effectively serves as a computationally efficient surrogate of the driving force for transgranular failure [47].

The band-averaged FIP informs a semi-empirical formulation for predicting the cracking of individual grains, which is based on the work by Tanaka and Mura [48]. This approach estimates number of cycles required to nucleate a crack on each band (N_{Nuc}) [12],

$$N_{Nuc} = \frac{\alpha_g}{d_{gr}} (\text{FIP}^\alpha)^{-2}, \quad 2$$

where α_g corresponds to the mechanical irreversibility, which depends strongly on the environment and loading conditions (e.g., cycling frequency). D_{GR} represents the grain cross section that becomes active when nucleating a crack. For each band we estimate D_{GR} by computing,

$$D_{GR} = D_{st} + \sum_1^n \omega^i D_{nd}^i, \quad 3$$

in which D_{st} is diameter of the band taken as the square root of its surface while the second term is the weighted sum (ω^i) of the diameters (D_{nd}^i) of all the bands in neighbouring grains having low disorientation (θ_{dis}^k) between the crystallographic orientations and is computed as

$$\omega^i = \left\langle 1 - \frac{\theta_{dis}^k}{20} \right\rangle. \quad 4$$

The Macaulay brackets satisfy that $(a) = a$ if $a > 0$, $(a) = 0$ if $a \leq 0$.

Hence, the minimum N_{Nuc} among all bands in all grains corresponds to the number of cycles required to crack the first grain. Next, we explore the attribution of the change in resonant frequency to cracking the first grain.

4. Results from Models and Experiments

First, we investigate the relation between the resonant frequency and the cracking of individual grains by considering synthetic microstructures with anisotropic elastic models achieved by artificially increasing the activation energy F_0 . In this way, we avoid force transients due to the evolution of plastic deformation and we resolve precisely the effect of cracking individual grains on the resulting forces. We applied a rotation of 25mrad and computed the total force applied before and after cracking those bands that resulted in the minimum life with Equation (**Error! Reference source not found.**) in the subsequent CPFEM analysis. The relative decrease in reaction force due to a cracked grain is equal to the relative decrease in rotational stiffness of the microbeam, k_θ , which is related to resonance frequency through [49],

$$f_0 = \frac{1}{2\pi} \sqrt{\frac{k_\theta}{J}} \quad 5$$

where f_0 is the resonant frequency, k_θ is the rotational stiffness, J is the polar moment of inertia.

Figure 7 shows a reduction in the reaction forces roughly between 0.5% and 2% upon cracking a single grain in 10 microstructural realizations with anisotropic elastic models. In addition, this reduction depends nonlinearly on the size of the grain cracked. According to Equation **Error! Reference source not found.**, a 0.5 to 2% decrease in reaction force

results in a 0.25 to 1% decrease in f_0 . Hence, these results support that a reduction about 1% decrease in resonant frequency from experiments is a good estimate for the first nucleation of a crack in a grain.

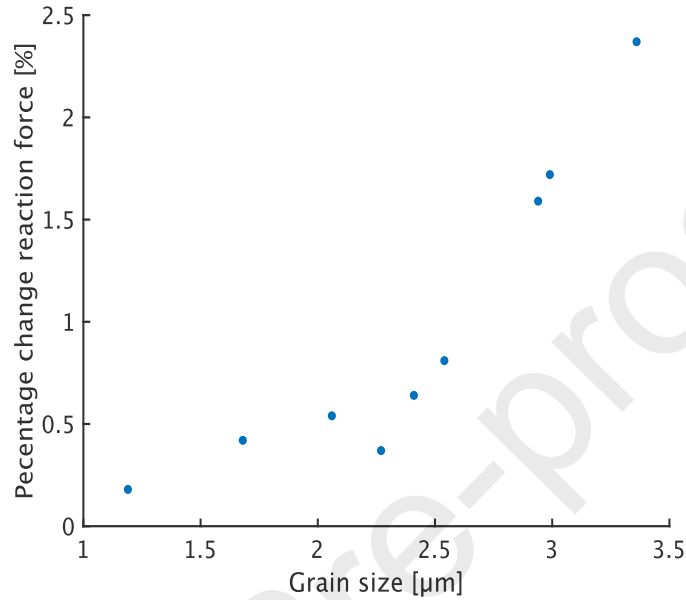


Figure 7. Percentage change in reaction forces upon cracking one grain in anisotropic elastic models. The change in force depends nonlinearly on the size of the slip plane cracked.

Next, we compute the minimum number of cycles to nucleate the first fatigue crack in a single grain from 20 synthetic microstructures using CPFEM. Since the gauge section represent one-fourth of the actual volume on the real microbeam, we present a fair comparison by considering the lowest quartile life results (hence, the five lowest life predictions).

Figure 8 presents the crack nucleation life results from the experiment and the CPFEM calculations (Equation **Error! Reference source not found.**), for different angle of rotations under vacuum and air. The experimental results correspond to the number of cycles required for a reduction in 1% of the resonant frequency. To estimate the crack

nucleation life for the respective environments, the α_g values based on Equation **Error! Reference source not found.** for the vacuum and air environments were estimated to be 1.0 and 0.00075 respectively. The results from 32 experiments and 60 CPFEM simulations overlap for loading amplitudes between 8 to 26 mrad. For completeness, Appendix B also presents the strain amplitude at the edge of the microbeam vs crack nucleation life curve.

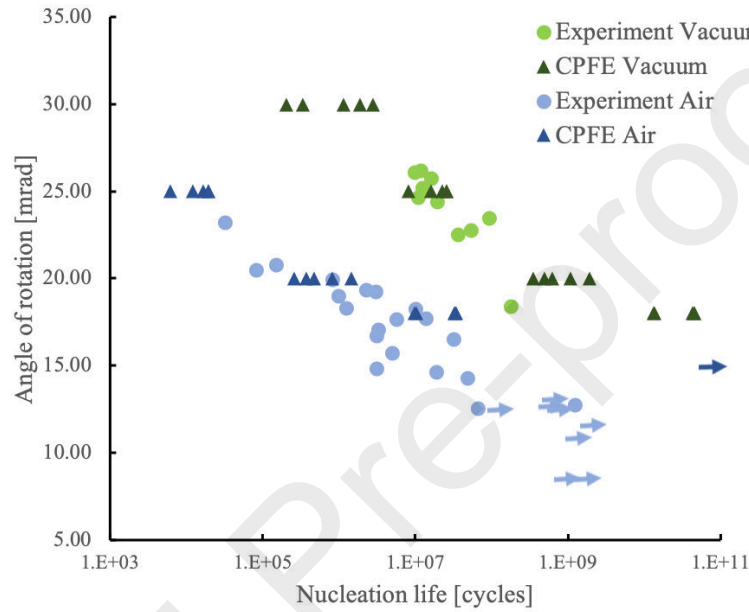


Figure 8. Predicted and experimental crack nucleation rotation-angle vs life curve for various rotations in vacuum and air environments. The arrows represent the runouts and the colours that correspond to the respective environments for experiment and CPFEM. For 18 mrad, three data points overlap on the logarithmic scale (total of 5 CPFEM per environment). A total of 32 experiments were performed using similar specimens and rotation angles from 8 to 26 mrad.

To further assess the predictive capability of the CPFEM damage model, we compare the number of cracks and location on the microbeam with models and experiments undergoing 25 mrad rotation in vacuum. We consider two experiments to quantify the number of cracks on a $200 \mu\text{m}^2$ area on the microbeam sidewall (see Figure 9a), which is equivalent to the crystal plasticity section on simulations. The accurate identification of cracks was possible thanks to the cross-sectioning of the microbeam with FIB (see Section

2.2). For simulations, we computed the density of cracks by quantifying the number of grains that present a band with an expected life below a target life. Upon increasing this target, larger number of grains would nucleate cracks as shown in Figure 9b, which compares the crack density from 20 microstructure realizations and two experiments. Overall, the experimental results fall within the variability predicted by the simulations.

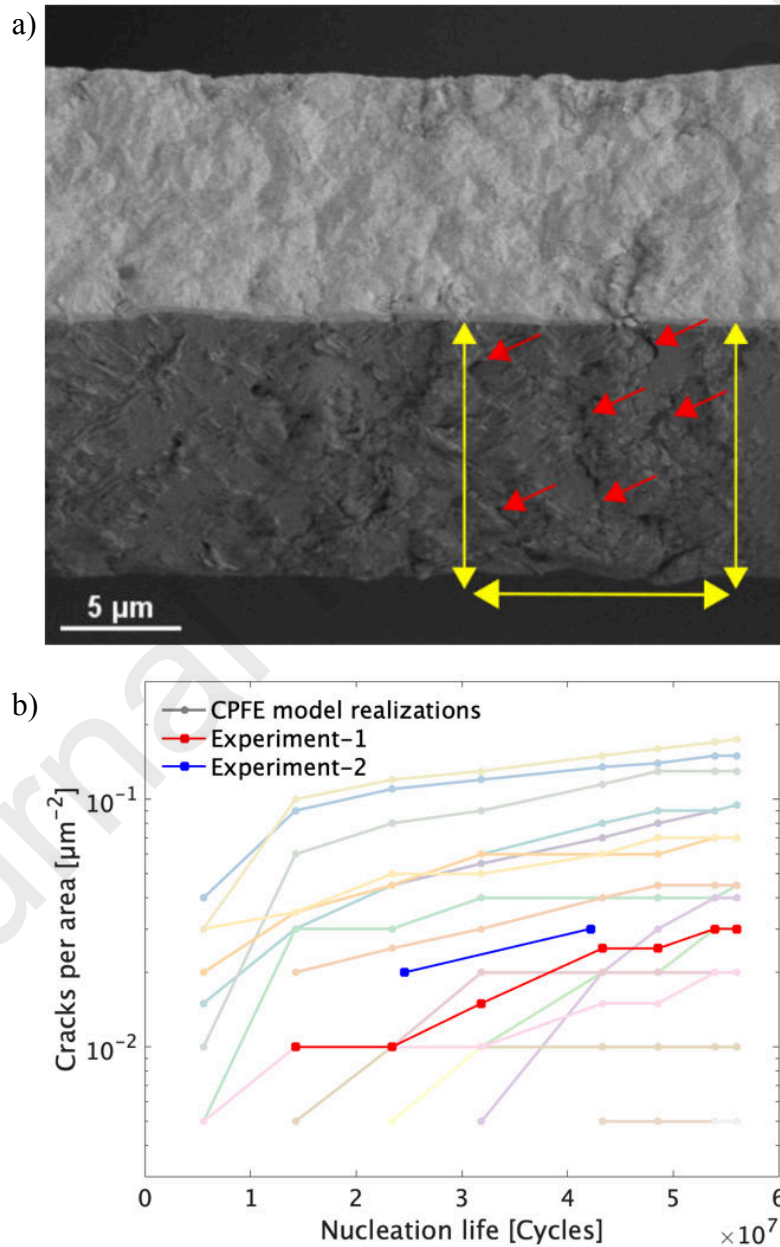


Figure 9. – (a) Inclined SEM image of one experimental microbeam indicating the location of transgranular cracks (b) Number of cracks per unit area for a rotation angle of 25mrad in a vacuum environment from 20 model realizations and two experiments.

Finally, we compare the orientation of cracks in models and experiments. First, we compute the orientation of the slip bands in Figure 10a and we compare with the orientation of the bands cracked in 20 model realisations. We measure the experimental slip localization from the sample in Figure 10a, for which the testing was stopped before abundant disruption of the surface (otherwise it would obscure the crack orientation). The empirical cumulative distribution functions (CDF) in Figure 10b shows that cracks predictions with models and in experiments overlap and are, in average, biased by almost 10° with respect to 45° , which would correspond to an isotropic response (maximum homogeneous shear). For comparison, we also performed 20 realizations with the same grain morphology, but using random crystallographic texture. These results are significantly different from experiments, which supports the predictive power of our computational approach.

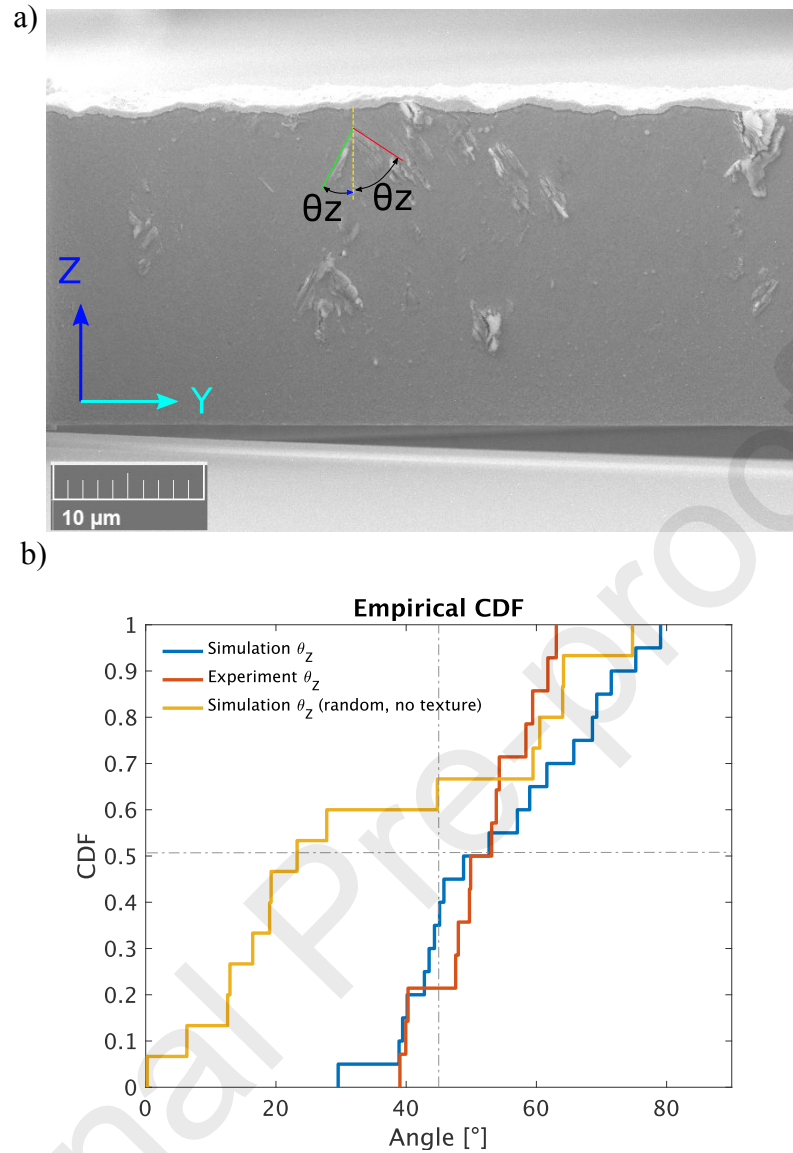


Figure 10. (a) SEM image showing several slip bands whose orientation with respect to the z-axis was measured. (b) A cumulative density function plot comparing the direction angles of the cracked grain slip plane normal to the Y and Z directions in the 20 microbeam microstructure realisations directions for the CPFEM simulations and experiments.

5. Discussion

The microstructural CPFEM framework implemented in this work has demonstrated its capability to predict transgranular fatigue damage at the microstructural level. A distinguishing feature of our approach is its ability to model the crack nucleation scatter

that arises from the limited number of grains strained on the microbeam without making any special provision or additional fitting of parameters. Furthermore, both the modelling and experimental approaches can be applied to other materials and loading configurations in which transgranular planar cracking dominates.

Our work has quantified the impact on fatigue failure of the relatively small dimensions of the MEMS compared to the microstructure. We demonstrated the ability of models to quantify the variability of the fatigue crack nucleation life, which is different for two MEMS. Similarly, Figure 9b has shown that the density of cracks strongly depends on the particular on the specific microstructure and crystallographic texture. Hence, these distributions are a function of the sample dimension, loading direction, microstructural attributes, etc.

We argue that two main characteristics of our model contribute to its predictive power. First, we considered a detailed reconstruction of the microstructure morphology, which provides the basis to model accurately volumes fractions that are prone to damage. Our approach to discretise the grain in bands provides a key capability to distinguish the planes more favourably aligned for transgranular damage in elongated grains deformed with a gradient. Indeed, there is a competition between the size of the grain plane, the most favourable orientation for damaging, the grain size, and the bending grain gradient that biases the nucleation of cracks to values lower than 45° , in average.

Secondly, our physics-based crystal plasticity model has been independently parameterized across scales to match Ni single- and poly-crystals. Compared to pure macroscopic Ni, only the parameterization of the glide barrier differs due to the strengthening of impurities, which results in a higher yield strength (monolithic FCC metals share similar mesoscale parameters). Since the system is deformed under rotation control, which is equivalent to strain control, a change in the yield stress affects mainly the

partition between the elastic and plastic deformation rather than the partition of plasticity across slip systems. The correct partition of plasticity, which is essential to capture texture effects, is conveyed from our earlier estimation [40] of mesoscale parameters from macroscopic Ni single crystal.

We also adjusted the fatigue irreversibility factor to account for the effect of the environment and the high deformation frequencies. This calibration affects the average life values, but has no significant effect on their variability. Thus, we argue that the scatter is not directly calibrated for, but it is an intrinsic result of reproducing the correct physics of microstructural attributes in the small MEMS volume.

We conclude emphasizing that predictive physics-based models benefit from the independent parameterization at multiple scales, from single and polycrystals data. A convoluted fitting approach in which multiple parameters are adjusted from the same experimental data set carries the risk of spurious cancellation error between parameters and limit the predictive power of models [50].

6. Conclusions

This work employs a 3D mesoscale CPFEM model to investigate the influence of microstructure heterogeneity on the crack nucleation in Ni microbeams. The predicted distributions of fatigue life for the microbeams subjected to the bending loads agree with the experiments even when there is no explicit calibration for the scatter. The location of the cracks on the simulated microbeams were also consistent with the experimental observations on experimental samples. This work demonstrates the predictive capability as well as the model ability to account for the influence of microstructure heterogeneity on the fatigue life in metals.

Acknowledgement

This work was supported primarily by the National Science Foundation (NSF) Award Number 1562499.

References

- [1] D.J. Fonseca, M. Sequera, On MEMS reliability and failure mechanisms, *Int. J. Qual. Stat. Reliab.* 2011 (2011).
- [2] J.A. Krogstad, C. Keimel, K.J. Hemker, Emerging materials for microelectromechanical systems at elevated temperatures, *J. Mater. Res.* 29 (2014) 1597–1608. <https://doi.org/10.1557/jmr.2014.183>.
- [3] G.-D. Sim, J.A. Krogstad, K.M. Reddy, K.Y. Xie, G.M. Valentino, T.P. Weihs, K.J. Hemker, Nanotwinned metal MEMS films with unprecedented strength and stability, *Sci. Adv.* 3 (2017) e1700685. <https://doi.org/10.1126/sciadv.1700685>.
- [4] B.L. Boyce, J.R. Michael, P.G. Kotula, Fatigue of metallic microdevices and the role of fatigue-induced surface oxides, *Acta Mater.* 52 (2004) 1609–1619.
- [5] E.K. Baumert, O.N. Pierron, Very high cycle fatigue crack initiation in electroplated Ni films under extreme stress gradients, *Scr. Mater.* 67 (2012) 45–48.
- [6] T. Straub, E.K. Baumert, C. Eberl, O.N. Pierron, A method for probing the effects of conformal nanoscale coatings on fatigue crack initiation in electroplated Ni films, *Thin Solid Films.* 526 (2012) 176–182.
- [7] S. Gupta, A. Barrios, N. England, O.N. Pierron, Improved very high cycle bending fatigue behavior of Ni microbeams with Au coatings, *Acta Mater.* 161 (2018) 444–455.
- [8] S. Burger, C. Eberl, A. Siegel, A. Ludwig, O. Kraft, A novel high-throughput fatigue testing method for metallic thin films, *Sci. Technol. Adv. Mater.* 12 (2011) 54202.
- [9] T. Straub, M.F. Berwind, T. Kennerknecht, Y. Lapusta, C. Eberl, Small-scale multiaxial setup for damage detection into the very high cycle fatigue regime, *Exp. Mech.* 55 (2015) 1285–1299.
- [10] D. Kiener, C. Motz, W. Grosinger, D. Weygand, R. Pippan, Cyclic response of copper single crystal micro-beams, *Scr. Mater.* 63 (2010) 500–503.
- [11] D.R. Sparks, M.I. Chia, G.Q. Jiang, Cyclic fatigue and creep of electroformed micromachines, *Sensors Actuators A Phys.* 95 (2001) 61–68.
- [12] C.P. Przybyla, D.L. McDowell, Microstructure-sensitive extreme value probabilities for high cycle fatigue of Ni-base superalloy IN100, *Int. J. Plast.* 26 (2010) 372–394.
- [13] S. Lucarini, J. Segurado, An upscaling approach for micromechanics based fatigue: from RVEs to specimens and component life prediction, *Int. J. Fract.* (2019). <https://doi.org/10.1007/s10704-019-00406-5>.
- [14] W.L. Chan, M.W. Fu, J. Lu, The size effect on micro deformation behaviour in

- micro-scale plastic deformation, *Mater. Des.* 32 (2011) 198–206.
- [15] D.L. McDowell, F.P.E. Dunne, Microstructure-sensitive computational modeling of fatigue crack formation, *Int. J. Fatigue*. 32 (2010) 1521–1542. <https://doi.org/doi: DOI: 10.1016/j.ijfatigue.2010.01.003>.
- [16] G.M. Castelluccio, D.L. McDowell, A mesoscale approach for growth of 3D microstructurally small fatigue cracks in polycrystals, *Int. J. Damage Mech.* 23 (2014). <https://doi.org/10.1177/1056789513513916>.
- [17] C.P. Przybyla, W.D. Musinski, G.M. Castelluccio, D.L. McDowell, Microstructure-sensitive HCF and VHCF simulations, *Int. J. Fatigue*. 57 (2013). <https://doi.org/10.1016/j.ijfatigue.2012.09.014>.
- [18] C.A. Sweeney, W. Vorster, S.B. Leen, E. Sakurada, P.E. McHugh, F.P.E. Dunne, The role of elastic anisotropy, length scale and crystallographic slip in fatigue crack nucleation, *J. Mech. Phys. Solids*. 61 (2013) 1224–1240. <https://doi.org/10.1016/j.jmps.2013.01.001>.
- [19] D.-F. Li, R.A. Barrett, P.E. O'Donoghue, N.P. O'Dowd, S.B. Leen, A multi-scale crystal plasticity model for cyclic plasticity and low-cycle fatigue in a precipitate-strengthened steel at elevated temperature, *J. Mech. Phys. Solids*. 101 (2017) 44–62.
- [20] G.M. Castelluccio, D.L. McDowell, Microstructure-sensitive small fatigue crack growth assessment: Effect of strain ratio, multiaxial strain state, and geometric discontinuities, *Int. J. Fatigue*. 82 (2016) 521–529.
- [21] H. Proudhon, J. Li, W. Ludwig, A. Roos, S. Forest, Simulation of Short Fatigue Crack Propagation in a 3D Experimental Microstructure, *Adv. Eng. Mater.* 19 (2017) 1600721. <https://doi.org/10.1002/adem.201600721>.
- [22] A. Rovinelli, M.D. Sangid, H. Proudhon, Y. Guilhem, R.A. Lebensohn, W. Ludwig, Predicting the 3D fatigue crack growth rate of small cracks using multimodal data via Bayesian networks: In-situ experiments and crystal plasticity simulations, *J. Mech. Phys. Solids*. 115 (2018) 208–229. <https://doi.org/https://doi.org/10.1016/j.jmps.2018.03.007>.
- [23] Y. Yang, N. Yao, B. Imasogie, W.O. Soboyejo, Nanoscale and submicron fatigue crack growth in nickel microbeams, *Acta Mater.* 55 (2007) 4305–4315. <https://doi.org/https://doi.org/10.1016/j.actamat.2007.03.027>.
- [24] J.A.R. Bomidi, N. Weinzapfel, F. Sadeghi, Three-dimensional modelling of intergranular fatigue failure of fine grain polycrystalline metallic MEMS devices, *Fatigue Fract. Eng. Mater. Struct.* 35 (2012) 1007–1021. <https://doi.org/10.1111/j.1460-2695.2012.01689.x>.
- [25] F. Sadeghi-Tohidi, O.N. Pierron, Extreme stress gradient effects on microstructural fatigue crack propagation rates in Ni microbeams, *Appl. Phys. Lett.* 106 (2015) 201904. <https://doi.org/10.1063/1.4921476>.
- [26] F. Sadeghi-Tohidi, O.N. Pierron, Towards prediction of the fatigue life of Ni microbeams under extreme stress gradients, *Extrem. Mech. Lett.* 9 (2016) 97–107.
- [27] S.W. Banovic, K. Barmak, A.R. Marder, Microstructural characterization and hardness of electrodeposited nickel coatings from a sulphamate bath, *J. Mater. Sci.* 33 (1998) 639–645. <https://doi.org/10.1023/A:1004321224586>.
- [28] A. Godon, J. Creus, X. Feaugas, E. Conforto, L. Pichon, C. Armand, C. Savall, Characterization of electrodeposited nickel coatings from sulphamate electrolyte without additive, *Mater. Charact.* 62 (2011) 164–173.

- [29] C. Savall, A. Godon, J. Creus, X. Feaugas, Influence of deposition parameters on microstructure and contamination of electrodeposited nickel coatings from additive-free sulphamate bath, *Surf. Coat. Technol.* 21 (2012) 4394–4402. <https://doi.org/10.1016/j.surfcoat.2012.04.068>.
- [30] S. Pathak, M. Guinard, M.G.C. Vernooij, B. Cousin, Z. Wang, J. Michler, L. Philippe, Influence of lower current densities on the residual stress and structure of thick nickel electrodeposits, *Surf. Coatings Technol.* 205 (2011) 3651–3657. <https://doi.org/10.1016/j.surfcoat.2011.01.012>.
- [31] A. Barrios, S. Gupta, G.M. Castelluccio, O.N. Pierron, Quantitative in Situ SEM High Cycle Fatigue: The Critical Role of Oxygen on Nanoscale-Void-Controlled Nucleation and Propagation of Small Cracks in Ni Microbeams, *Nano Lett.* 18 (2018) 2595–2602. <https://doi.org/10.1021/acs.nanolett.8b00343>.
- [32] Y. Guilhem, S. Basseville, F. Curtit, J.-M. Stéphan, G. Cailletaud, Numerical analysis of the effect of surface roughness on mechanical fields in polycrystalline aggregates, *Model. Simul. Mater. Sci. Eng.* 26 (2018) 45004. <https://doi.org/10.1088/1361-651x/aab217>.
- [33] E.K. Baumert, O.N. Pierron, Fatigue Degradation Properties of LIGA Ni Films Using Kilohertz Microresonators, *J. Microelectromechanical Syst.* 22 (2013) 16–25. <https://doi.org/10.1109/JMEMS.2012.2212422>.
- [34] T.E. Buchheit, J.R. Michael, T.R. Christenson, D.A. LaVan, S.D. Leith, Microstructural and mechanical properties investigation of electrodeposited and annealed LIGA nickel structures, *Metall. Mater. Trans. A.* 33 (2002) 539–554.
- [35] S.H. Goods, R.P. Janek, T.E. Buchheit, J.R. Michael, P.G. Kotula, Oxide dispersion strengthening of nickel electrodeposits for microsystem applications, *Metall. Mater. Trans. A.* 35 (2004) 2351–2360.
- [36] T. Borca-Tasciuc, D.-A. Borca-Tasciuc, S. Graham, S.H. Goods, J.J. Kelly, N.Y.C. Yang, Annealing effects on mechanical and transport properties of Ni and Ni-alloy electrodeposits, *J. Microelectromechanical Syst.* 15 (2006) 1051–1059.
- [37] M.A. Groeber, M.A. Jackson, DREAM. 3D: a digital representation environment for the analysis of microstructure in 3D, *Integr. Mater. Manuf. Innov.* 3 (2014) 5.
- [38] B. Chen, J. Jiang, F.P.E. Dunne, Microstructurally-sensitive fatigue crack nucleation in Ni-based single and oligo crystals, *J. Mech. Phys. Solids.* 106 (2017) 15–33. <https://doi.org/10.1016/j.jmps.2017.05.012>.
- [39] G.M. Castelluccio, D.L. McDowell, Mesoscale modeling of microstructurally small fatigue cracks in metallic polycrystals, *Mater. Sci. Eng. A.* 598 (2014). <https://doi.org/10.1016/j.msea.2014.01.015>.
- [40] G.M. Castelluccio, D.L. McDowell, Mesoscale cyclic crystal plasticity with dislocation substructures, *Int. J. Plast.* 98 (2017). <https://doi.org/10.1016/j.ijplas.2017.06.002>.
- [41] E. Kakandar, G.M. Castelluccio, A. Barrios, O. Pierron, X. Maeder, Computational and experimental study of crack initiation in statistical volume elements, *MATEC Web Conf.* 300 (2019) 10001. <https://doi.org/10.1051/mateconf/201930010001>.
- [42] ABAQUS. FEM Software V2017, ABAQUS. FEM Software 2017, (2009).
- [43] F. Dalla Torre, P. Spätig, R. Schäublin, M. Victoria, Deformation behaviour and microstructure of nanocrystalline electrodeposited and high pressure torsioned nickel, *Acta Mater.* 53 (2005) 2337–2349.

- [44] V. Maier, K. Durst, J. Mueller, B. Backes, H.W. Höppel, M. Göken, Nanoindentation strain-rate jump tests for determining the local strain-rate sensitivity in nanocrystalline Ni and ultrafine-grained Al, *J. Mater. Res.* 26 (2011) 1421–1430.
- [45] G.M. Castelluccio, W.D. Musinski, D.L. McDowell, Computational micromechanics of fatigue of microstructures in the HCF–VHCF regimes, *Int. J. Fatigue*. 93 (2016) 387–396. <https://doi.org/10.1016/j.ijfatigue.2016.05.019>.
- [46] Fatem, Ali, D.F. Socie, A critical plane approach to multiaxial fatigue damage including out-of-phase loading, *Fatigue Fract. Eng. Mater. Struct.* 11 (1988) 149–165.
- [47] G.M. Castelluccio, D.L. McDowell, Microstructure and mesh sensitivities of mesoscale surrogate driving force measures for transgranular fatigue cracks in polycrystals, *Mater. Sci. Eng. A*. 639 (2015) 626–639. <https://doi.org/10.1016/j.msea.2015.05.048>.
- [48] D. Kuhlmann-Wilsdorf, A Dislocation Model for Fatigue Crack Initiation, *J. Appl. Mech.* 48 (1981) 97–103.
- [49] R.E. Blake, Basic vibration theory, *Harris' Shock Vib. Handbook*, S. (1987) 1–2.
- [50] A. Rovinelli, Y. Guilhem, H. Proudhon, R.A. Lebensohn, W. Ludwig, M.D. Sangid, Assessing reliability of fatigue indicator parameters for small crack growth via a probabilistic framework, *Model. Simul. Mater. Sci. Eng.* 25 (2017) 45010. <https://doi.org/10.1088/1361-651x/aa6c45>.
- [51] U. Kocks, Argon AS, Ashby M, *Thermodynamics Kinet. Slip.* (1975) 74.
- [52] U.F. Kocks, H. Mecking, Physics and phenomenology of strain hardening: the FCC case, *Prog. Mater. Sci.* 48 (2003) 171–273. [https://doi.org/10.1016/S0079-6425\(02\)00003-8](https://doi.org/10.1016/S0079-6425(02)00003-8).
- [53] Kuhl, A new theory of work hardening in crystals, *Trans. Met. Soc. AIME*. 218 (1962) 962.
- [54] M. Sauzay, L.P. Kubin, Scaling laws for dislocation microstructures in monotonic and cyclic deformation of fcc metals, *Prog. Mater. Sci.* 56 (2011) 725–784. <https://doi.org/10.1016/j.pmatsci.2011.01.006>.
- [55] L.P. Kubin, G. Canova, M. Condat, B. Devincere, V. Pontikis, Y. Bréchet, Dislocation Microstructures and Plastic Flow: A 3D Simulation, *Solid State Phenom.* 23–24 (1992) 455–472. <https://doi.org/10.4028/www.scientific.net/SSP.23-24.455>.
- [56] M. Verdier, M. Fivel, I. Groma, Mesoscopic scale simulation of dislocation dynamics in fcc metals: Principles and applications, *Model. Simul. Mater. Sci. Eng.* 6 (1998) 755. <https://doi.org/10.1088/0965-0393/6/6/007>.
- [57] C. Zhou, S.B. Biner, R. LeSar, Discrete dislocation dynamics simulations of plasticity at small scales, *Acta Mater.* 58 (2010) 1565–1577. <https://doi.org/10.1016/j.actamat.2009.11.001>.
- [58] G.M. Castelluccio, C.B. Geller, D.L. McDowell, A rationale for modeling hydrogen effects on plastic deformation across scales in FCC metals, *Int. J. Plast.* 111 (2018) 72–84. <https://doi.org/10.1016/J.IJPLAS.2018.07.009>.
- [59] F. Ashraf, G.M. Castelluccio, Estimation of dislocation glide barrier in FCC metals and alloys, *Under Rev.* (2020).

Appendix A

Figure 13 shows the crack path, along with the EBSD Scans, of one cross-section of the sample shown in Figure 2. Similarly, Figure 14 shows the crack path of the sample shown in Figure 9.

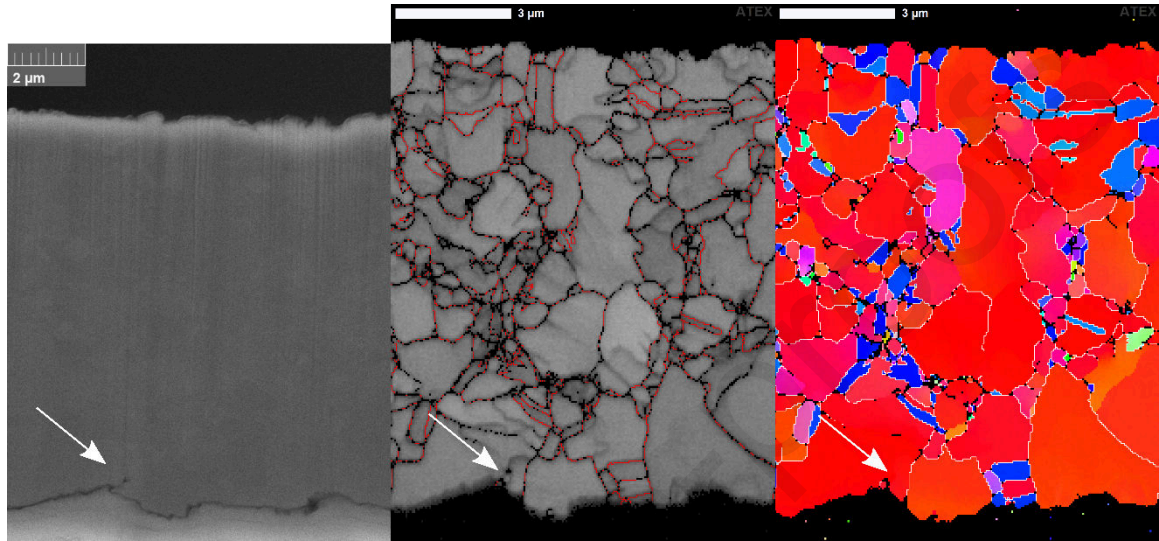


Figure 13. Transgranular crack path for sample in Figure 2

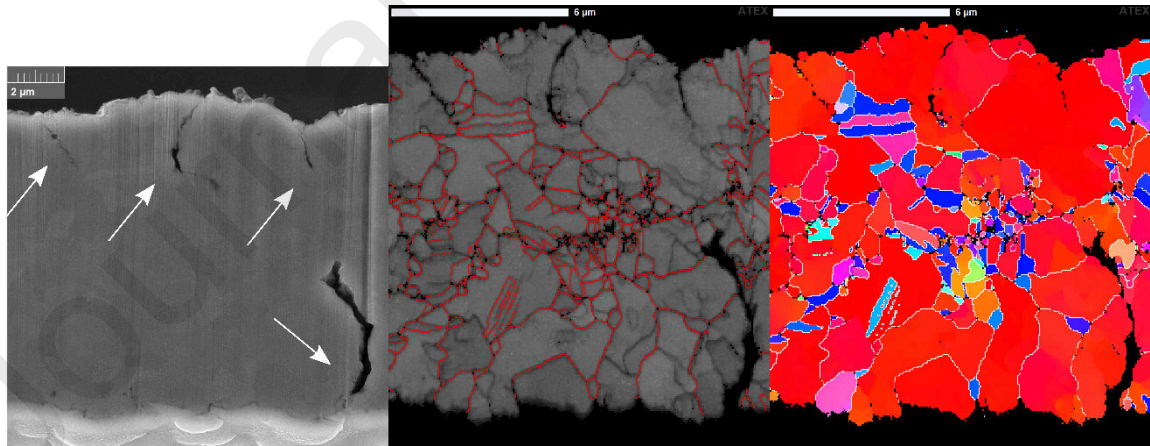


Figure 14. Transgranular cracks (upper cracks) and mixed mode (bottom crack) cracks for sample in Figure 9

Appendix B.

For completeness, Figure 11 presents the relation between the maximum strain and angle of rotation computed with elasto-plastic isotropic model while Figure 12 present the corresponding strain vs life curve.

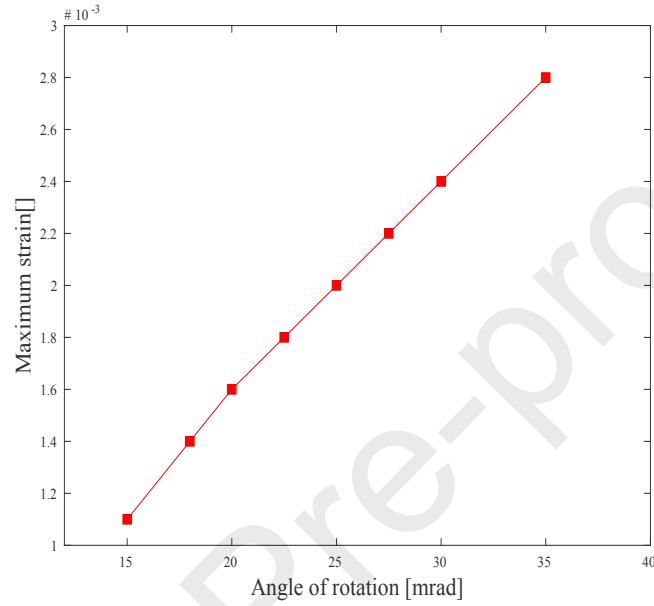


Figure 11. Maximum strain as a function of the angle of rotation computed from simulation with isotropic elasto-plastic model.

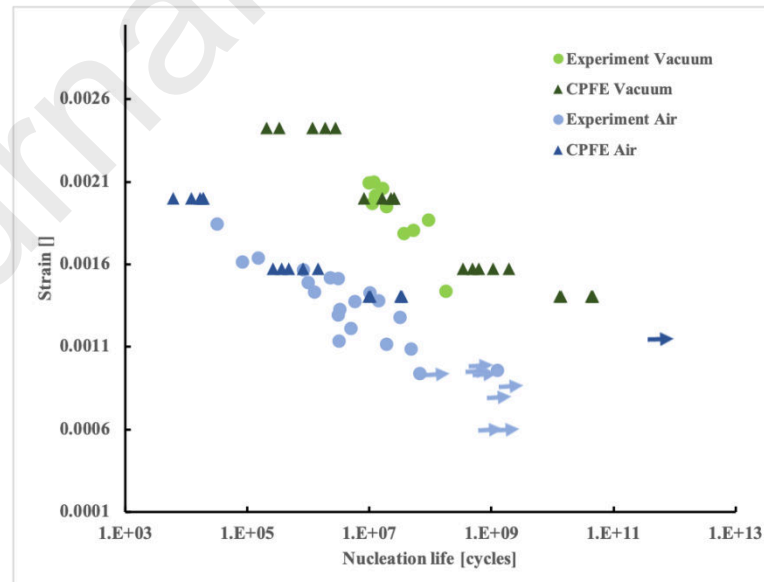


Figure 12. Strain vs life curve in vacuum and air environments from models and experiments.

Appendix C

The crystal plasticity formulation employs a rate-dependent flow rule introduced by Kocks et al. [51] i.e.,

$$\dot{\gamma}^{\alpha} = \rho_m^s \bar{l} b v_G \exp\left(-\frac{\Delta G(\tau_{eff}^{\alpha})}{k_B T}\right) \text{sgn}(\tau^{\alpha} - B^{\alpha}). \quad 6$$

Here, \bar{l} represents the dislocation mean free path, ρ_m^s corresponds to the mobile dislocations density, B is the Burgers vector $\sim 2.5 \times 10^{-10}$ m, v_G is the dislocation attempt frequency $\sim 10^{12}$ s⁻¹, T is the absolute temperature and k_B is Boltzmann constant. Furthermore, ΔG is the Gibbs energy required to bypass point obstacles, τ_{eff}^{α} is the effective stress and B^{α} is the slip system back stress.

The Gibbs energy corresponding to the glide barrier has been parameterised as [51,52],

$$\Delta G(\tau_{eff}^{\alpha}) = F_0 \left(1 - \left[\frac{\tau_{eff}^{\alpha}}{S_t^0 \frac{\mu}{\mu_0}} \right]^p \right)^q, \quad 7$$

in which F_0 is the activation energy, and p, q are profile parameters, S_t^0 is thermal slip resistance at 0 K, and μ and μ_0 are the shear modulus (C44) at temperatures T and 0K, respectively. The effective stress, which stress drives the dislocation glide, depends on the back stress and threshold stress, S^{α} ,

$$\tau_{eff}^{\alpha} = \langle |\tau^{\alpha} - B^{\alpha}| - S^{\alpha} \rangle \quad 8$$

in which τ^{α} is the resolved shear stress for slip system α , and $\langle \rangle$ correspond to the Macaulay brackets.

The threshold stress is given by,

$$S^{\alpha} = \alpha_{LE} \frac{\mu b}{(1 - f_w) d_{struct}} + \mu b (A_{ii} \rho^{\alpha})^{1/2}, \quad 9$$

in which the first term corresponds to the stress required to bow out a dislocation and the

second term is self-interaction strength. Here, α_{LE} is the dislocation line energy, and f_w is the dislocation wall fraction, which depends on the maximum plastic shear strain range per cycle,

$$f_w = f_{inf}(f_0 - f_{inf})\exp\left(\frac{-\Delta\gamma^{max}/2}{g_p}\right) \quad 10$$

with f_{inf} , f_0 , and g_p material parameters informed from dislocations structures.

The back stress incorporates dislocation substructure effects by leveraging on a mean field formulation based on Eshelby approach[40],

$$\dot{B}^\alpha = \frac{f_w}{1 - f_w} \frac{2\mu(1 - 2S_{1212})}{1 + 4S_{1212}\mu f_{Hill}} \dot{\gamma}^\alpha, \quad 11$$

where S_{1212} correspond the Eshelby tensor component for a prolate spheroid, η corresponds to the normalized dislocation mean free path. The Hill factor, f_{Hill} , corresponds to the instantaneous macroscopic plastic deformation tangent and carries a dependence on the mean grain size, d_{gr} [40],

$$f_{Hill} = \tanh\left(\frac{0.005d_{gr}}{d_{struct}}\right) \frac{d\gamma^\alpha}{dt^\alpha} \quad 12$$

This factor accounts for the potential for plastic accommodation and depends on the relative size between mesoscale dislocation structures (which change with load) and grains/crystals.

Extensive experimental results have demonstrated that dislocation substructures follow the similitude principle, which the characteristic dislocation substructure distance, d_{struct} , is inversely propotional to the shear stress, [53,54],

$$d_{struct} = K_{struct}\mu(T)b \quad 13$$

and the proportionality factor K_{struct} ranges between 2 and 4 form most FCC metals under cyclic loading.

Dislocation mean glide distance is anisotropic and depends on the dislocation substructure formed upon cycling as proposed in [40]. Thus, we consider that \bar{l} is proportional to d_{struct} and the proportionality factor η ranges from 1 for cells to 25 for persistent slip bands,

$$\bar{l} \approx l_{struct} = \eta d_{struct} \quad 14$$

For further details about the identification of the dislocation structure please refer to [40].

We compute the mobile dislocation density on slip system α as a balance between dislocation multiplication, annihilation and cross slip,

$$\dot{\rho}_m^{s\alpha} = \frac{k_{multi}}{b l_{struct}} |\dot{\gamma}^\alpha| - \frac{2\gamma_s^{edge}}{b} \rho_m^{s\alpha} |\dot{\gamma}^\alpha| - \gamma \frac{2|\dot{\tau}^\alpha - \dot{B}^\alpha|}{\mu b d_{struct}} |^{Unload} + \dot{\rho}_{cs}^s |^{\zeta \rightarrow \alpha} - \dot{\rho}_{cs}^s |^{\alpha \rightarrow \zeta} \quad 15$$

in which $k_{multi} = 1$ for cell structures and $k_{multi} = 2$ for parallel walls such as PSBs and labyrinth, $\gamma = 1$ if $sgn(\dot{\tau}^\alpha - \dot{B}^\alpha) \neq sgn(\tau^\alpha - B^\alpha)$ or $\dot{\gamma}^\alpha = 0$; otherwise $\gamma = 0$ and $\dot{\rho}_{annih}^s |^{\alpha} |^{Unload} = 0$.

The term $\dot{\rho}_{cs}^s |^{\alpha \rightarrow \zeta}$ represents the mobile dislocation cross slip rate from plane α to ζ , and it follows a probabilistic approach proposed elsewhere [55–57], but considers the back stress to account for shielding effects of dislocation structures, i.e.,

$$\dot{\rho}_{cs}^{s\alpha} = -v \frac{l_{CS}}{d_0} \rho_m^{s\alpha} e^{\left(-v_{CS} \frac{\tau_{III} - |\tau^\zeta - B^\zeta|}{k_B T} \right)} \quad 16$$

Here, $l_{CS} \approx d_{struct}$ and $v \approx 1 s^{-1}$ are the dislocation length and the cross slip characteristic frequency, respectively. The cross slip activation volume is inversely proportional to the slip system shear stress, i.e.

$$V_{CS}^\alpha = \frac{1000 b^3 MPa}{|\tau^\alpha|} \quad 17$$

The critical cross slip stress, τ_{III} , is inversely proportional to the annihilation distance of

screw dislocations, y_s^{screw} ,

$$\tau_{III} = \frac{\mu b}{4\pi y_s^{screw}}$$

18

All parameters are summarized in Table 1 to Table 4 and agree with those presented earlier for pure Ni [40], except for the glide activation energy, which was increased to account for the solid solution strengthening of impurities as proposed before by the authors [58]. Further details about the choice of these parameters in the presence of solid solution strengthening impurities can be found elsewhere [59].

Table 1. Direct parameters for pure Ni

T						@0K	
293K	$10^{13}s^{-1}$	2.5×10^{-10}	251GPa	150GPa	124GPa	131.7GPa	87.02GPa

Table 2. Parameters related to atomistic scale unit processes for pure Ni

		p	q						
2.0ev	50MPa	0.6666	1.5	2nm	50nm	0.1	1.45	$1000b^3$	0.65

Table 3. Parameters associated with mesoscale dislocation structures for pure Ni

1	5	20	20	3.5	2	1	0.25	0.5	1.25

Table 4. Initial values for internal state variables for pure Ni

$2 \times 10^{12}m^{-2}$	$10\mu m$		25	0.25	$1000b^3$

- Integrating physics-based models for predicting fatigue crack nucleation
- Modelling and experiments in small volumes.
- Validation of crack nucleation orientation and nucleation life statistical distribution.
- Use of non-local FIPs in microstructure-sensitive models with gradients.